Weierstraß-Institut
für Angewandte Analysis und Stochastik
Leibniz-Institut im Forschungsverbund Berlin e. V.

Two-phase flows for sedimentation of suspensions

Dirk Peschka[1], Matthias Rosenau[2]

submitted: July 27, 2020

[1] Weierstrass Institute Mohrenstr. 39 10117 Berlin Germany E-Mail: dirk.peschka@wias-berlin.de	[2] Helmholtz Centre Potsdam GFZ German Research Centre for Geosciences Telegrafenberg 14473 Potsdam Germany E-Mail: rosen@gfz-potsdam.de

Two-phase flows for sedimentation of suspensions

Dirk Peschka, Matthias Rosenau

Abstract

We present a two-phase flow model that arises from energetic-variational arguments and study its implication for the sedimentation of buoyant particles in a viscous fluid inside a Hele-Shaw cell and also compare corresponding simulation results to experiments. Based on a minimal dissipation argument, we provide a simplified 1D model applicable to sedimentation and study its properties and the numerical discretization. We also explore different aspects of its numerical discretization in 2D. The focus is on different possible stabilization techniques and their impact on the qualitative behavior of solutions. We use experimental data to verify some first qualitative model predictions and discuss these experiments for different stages of batch sedimentation.

1 Introduction

Sedimentation and settling processes, i.e., flows where particles are transported in or separated from a suspending liquid phase, are relevant for geological processes such as sediment transport in rivers, lakes and oceans but also for technological applications such as water engineering and mineral processing, for example. This requires a fundamental understanding of the sediment transport in bodies of water [1] and of the dewatering processes [2]. A key concept for modeling settling processes is hindered settling [3, 4], which accounts for the reduction of the settling flux due to particle interactions as a function of the solid particle volume fraction $0 \leq \phi_{\mathrm{s}} \leq 1$ and has become an essential ingredient of most continuum models for suspension flows.

The seminal work of Kynch [5] introduced the mathematical study of sedimentation based on first-order nonlinear hyperbolic conservation laws $\partial_t \phi_{\mathrm{s}} + \partial_z f(\phi_{\mathrm{s}}) = 0$ with $\phi_{\mathrm{s}}(t,z)$ the solid volume fraction $\phi_{\mathrm{s}} : [0,T] \times \mathbb{R} \to [0,1]$ depending on time t and space z. This approach is widely used and allows for a systematic inclusion of hindered settling into the particle fluxes f. For a historical account of sedimentation research related to Kynch's work we refer to the work by Bürger and Wendland [6]. Many works suggested improvements of the Kynch theory and mathematical methods for the improved determination from the flux from experiments have been developed, see [7] for an introduction to flux identification. While batch sedimentation experiments have been performed for over a century, a more rigorous theoretical understanding has only been developed more recently (and still is) – for a review of theoretical and experimental findings see [8]. For simulation approaches considering sedimentation using discretely resolved particles we refer to [9, 10] and in particular [11] for the review on results for the associated Rayleigh-Taylor instability. Simulation approaches based on two-phase flow models with volume fractions (Euler-Euler models) are considered in [12–15].

In higher dimensions and for more complex flow geometries, in addition to hindered settling other effects become relevant. Acrivos and Leighton [16, 17] introduced shear induced migration as a fundamental contribution to the particle flux that facilitates transport opposed to gradients of shear rates and gradients of the viscosity caused by irreversible interparticle interactions. The impact of anisotropic normal stresses in corresponding continuum mechanical models was discussed by Morris and Boulay

[18]. Motivated by observations for dense granular flows [19] a similar universal behavior for pressure-imposed suspension flows was found by Boyer [20]. It is argued that the universality is generated by the viscoplastic behavior of dense suspensions near the jamming transition. The impact of shear induced migration on suspension flows down inclines was investigated in [21]. There is a large set of literature on homogenized models for the sedimentation of dilute suspensions, for recent advances we refer to [22, 23] and references therein.

The outline for this manuscript is as follows. First, we introduce and discuss a two-phase flow model which incorporates normal pressures necessary to have shear induced migration in a variational framework [24, 25]. Specifically for sedimentation, we reduce the variational model to a 1D model including the solid volume fraction and velocity field. We investigate the numerical discretization of this model and study the qualitative behavior of its solutions. We generalize this model to higher dimensions, where additionally we need to discuss different regularization techniques that are suggested by the saddle-point structure of the corresponding suspension flow model [26]. These theoretical findings are compared to sedimentation experiments in a non-Brownian suspension of spherical monodisperse particles in a viscous Newtonian fluid. We distinguish different regimes in the settling process, where predictions differ qualitatively and either more accurate material data or higher-dimensional models are required.

2   Two-phase suspension model

Thermodynamic approaches are well-developed for multiphase flows, e.g. see [25, 27–29], and the construction of corresponding frameworks is based on conservation laws and thermodynamic relations. Resulting systems of partial differential equations are thermo-mechanical-consistent models that reflect certain properties of the microscopic models when taking continuum limits. While thermodynamic considerations are clearly relevant for colloidal suspensions, e.g. [30], similar energetic variational structures should also be relevant for continuum models of noncolloidal suspensions and granular media [31]. In the following we consider binary suspensions of liquid and solid particles with respective volume fractions $0 \leq \phi_\ell, \phi_s \leq 1$ and $\phi_\ell + \phi_s = 1$. In particular, when neglecting kinetic energy and other sources of internal energy, the graviational free energy of an isothermal suspension in a container $\Omega \subset \mathbb{R}^d$ with $\mathbf{x} = (x, z) \in \Omega$ and $x \in \mathbb{R}^{d-1}$ and $z \in \mathbb{R}$ depending on $\phi_s(t, \mathbf{x})$ is

$$E_{\text{grav}}(\phi_s) = \int_\Omega \big(\varrho_s \phi_s + \varrho_\ell (1 - \phi_s)\big) gz \, \mathrm{d}x \, \mathrm{d}z, \tag{1}$$

and the energy should not increase in time, i.e., $\frac{\mathrm{d}}{\mathrm{d}t} E_{\text{grav}} \leq 0$. Note that we write E_{grav} as a function of ϕ_s alone, since the dependence on ϕ_ℓ can always be included by replacing $\phi_\ell = 1 - \phi_s$. In this expression $g = 9.81 \, \mathrm{m\,s^{-2}}$ is the gravitational acceleration and ϱ_s, ϱ_ℓ are the constant mass densities of solid and liquid, where we consider buoyant suspensions with heavier particles $\varrho_s > \varrho_\ell$.

While the densities are binary $\phi_s + \phi_\ell = 1$, the evolution in time $t \in [0, T]$ and space $\mathbf{x} \in \Omega \subset \mathbb{R}^d$ of both phases $\phi_s, \phi_\ell : [0, T] \times \Omega \to [0, 1]$ are goverened by a corresponding set of continuity equations

$$\partial_t \phi_s + \nabla \cdot (\phi_s \mathbf{u}_s) = 0, \tag{2a}$$

$$\partial_t \phi_\ell + \nabla \cdot (\phi_\ell \mathbf{u}_\ell) = 0, \tag{2b}$$

with the velocities $\mathbf{u}_s, \mathbf{u}_\ell : [0, T] \times \Omega \to \mathbb{R}^d$ of solid and liquid phase. While the two velocities are independent variables, they need to satisfy the additional constraint

$$\nabla \cdot \big(\phi_s \mathbf{u}_s + \phi_\ell \mathbf{u}_\ell\big) = 0, \tag{2c}$$

so that the suspension remains binary. With gravitational energy E_{grav} generating the driving force, the velocities obey the quasistatic momentum balances

$$-\nabla \cdot \tau_{\mathrm{s}}(\mathbf{u}_{\mathrm{s}}) + M(\mathbf{u}_{\mathrm{s}} - \mathbf{u}_{\ell}) = \phi_{\mathrm{s}} \nabla (p - f_{\mathrm{s}}),$$
$$-\nabla \cdot \tau_{\ell}(\mathbf{u}_{\ell}) - M(\mathbf{u}_{\mathrm{s}} - \mathbf{u}_{\ell}) = \phi_{\ell} \nabla p, \tag{2d}$$

where $f_{\mathrm{s}} = \frac{\delta E_{\text{grav}}}{\delta \phi_{\mathrm{s}}} = (\varrho_{\mathrm{s}} - \varrho_{\ell}) g z$ and $p : Q_T \to \mathbb{R}$ is the Lagrange multiplier for the constraint (2c). For this work we assume homogeneous Dirichlet boundary conditions for the velocities at $(0, T) \times \partial \Omega$. The stress tensors for solid and liquid stress τ_{s} and τ_{ℓ} are related to a possibly nonsmooth convex dissipation potential $\mathcal{R} = \mathcal{R}_{\mathrm{s}} + \mathcal{R}_{\ell} + \mathcal{R}_{\text{interact}}$ via $\tau_{\mathrm{s}} = \partial_{\mathbf{u}_{\mathrm{s}}} \mathcal{R}_{\mathrm{s}}(\mathbf{u}_{\mathrm{s}}; \phi_{\mathrm{s}})$ and $\tau_{\ell} = \partial_{\mathbf{u}_{\ell}} \mathcal{R}_{\ell}(\mathbf{u}_{\ell}; \phi_{\mathrm{s}})$, where for smooth potentials $\partial_{\mathbf{u}}$ is to be understood as the usual first variation and for nonsmooth convex potentials as the subdifferential with respect to $\mathbf{u}$. Using the symmetric gradient $e(\mathbf{u}_i) = \frac{1}{2}(\nabla \mathbf{u}_i + \nabla \mathbf{u}_i^\top)$ we have

$$\mathcal{R}_i(\mathbf{u}_i; \phi_{\mathrm{s}}) = \int_{\Omega} R_i(e(\mathbf{u}_i); \phi_{\mathrm{s}}) \, \mathrm{d}x \, \mathrm{d}z, \tag{2e}$$

$$\mathcal{R}_{\text{interact}}(\mathbf{u}_{\mathrm{s}}, \mathbf{u}_{\ell}; \phi_{\mathrm{s}}) = \int_{\Omega} M(\phi_{\mathrm{s}}) |\mathbf{u}_{\mathrm{s}} - \mathbf{u}_{\ell}|^2 \, \mathrm{d}x \, \mathrm{d}z, \tag{2f}$$

with a viscosity function $R_i : \mathbb{R}_{\text{sym}}^{d \times d} \times \mathbb{R} \to \mathbb{R}$ implying the necessary convexity for $\mathcal{R}_i$ and an interphase friction $M : \mathbb{R} \to \mathbb{R}$ with $R_i, M \geq 0$ for $i \in \{s, \ell\}$.

For compressible flows one often finds quadratic dissipation potentials such as

$$R_{\ell}(e, \phi) = \mu_{\ell}(\phi) [\mathrm{dev}(e)]^2 + \lambda_{\ell}(\phi) [\mathrm{trace}(e)]^2, \tag{3}$$

where μ_{ℓ} denotes the shear viscosity and λ_{ℓ} is the volume viscosity and both are increasing functions of the liquid concentration. The operator $\mathrm{dev}\, e = e - d^{-1}(\mathrm{trace}\, e)\mathbb{I}_d$ is the deviatoric part of e. For the solid phase stress we allow also for nonsmooth convex potentials here, which in addition to terms already present in the liquid viscosity could include terms of the form $(e : e)^{1/2} |\mathrm{trace}(e)|$ or similar. The term $\mathcal{R}_{\text{interact}}$ generates an interaction between solid and fluid flow. With smooth quadratic potentials we have

$$\frac{\mathrm{d}}{\mathrm{d}t} E_{\text{grav}}(\phi_{\mathrm{s}}) = -\mathcal{R}(\mathbf{u}_{\mathrm{s}}, \mathbf{u}_{\ell}; \phi_{\mathrm{s}}) \leq 0. \tag{4}$$

The analytical treatment of such models is difficult due to the loss of coercivity in the viscosity, since $R_s \to 0$ as $\phi_{\mathrm{s}} \to 0$. It is an interesting question for which type of dissipation $\mathcal{R}$ and free energy E one can guarantee what the densities stay nonnegative (or even positive) for nonnegative (or positive) initial data. While we do not attempt to prove this property here, we generally observe that even for moderately small time steps the numerical approximations of the volume fractions satisfy $-C \leq \phi_{\mathrm{s}}, \phi_{\ell} \leq 1 + C$ with $C \sim 10^{-4}$.

3 Sedimentation model

Now we discuss the simplification of the two-phase flow model (2) to a model for sedimentation. Therefore, let $\Omega = \mathbb{R} \times (0, L)$ and assume translational symmetry in in the first coordinate of $(x, z) = \mathbf{x} \in \Omega$. Therefore, the constraint (2c) reduces to $\partial_z(\phi_{\mathrm{s}} \mathbf{u}_{\mathrm{s}} + \phi_{\ell} \mathbf{u}_{\ell}) = 0$ and using the no-slip boundary conditions it can be directly integrated in z and becomes $\phi_{\mathrm{s}} \mathbf{u}_{\mathrm{s}} + \phi_{\ell} \mathbf{u}_{\ell} = 0$. For a binary mixture with

a maximal packing $0 < \phi_{\text{crit}} < 1$ we have $\phi_{\text{s}} \leq \phi_{\text{crit}}$ and thereby the liquid volume fraction is strictly positive $\phi_\ell \geq (1 - \phi_{\text{crit}}) > 0$. Hence, we can divide by ϕ_ℓ and can replace the liquid velocity by

$$u_\ell(t, z) = -\frac{\phi_{\text{s}}}{\phi_\ell} u_{\text{s}}(t, z), \tag{5}$$

with $\phi_\ell = 1 - \phi_{\text{s}}$. In one dimension, we assume a smooth quadratic dissipation of the form $R_\ell = \hat{\mu}_\ell(\phi_{\text{s}})(u'_{\text{s}})^2$ and $R_{\text{s}} = \hat{\mu}_{\text{s}}(\phi_{\text{s}})(u'_\ell)^2$, where we use the abbreviations $u'_{\text{s}} = \partial_z u_{\text{s}}$ and $u'_\ell = \partial_z u_\ell$. For the total dissipation using the expression (5) we obtain

$$\mathcal{R}(u_s; \phi_{\text{s}}) = \int_0^L \left[\hat{\mu}_\ell\left(\left(\tfrac{\phi_{\text{s}}}{\phi_\ell} u_{\text{s}}\right)'\right)^2 + \hat{\mu}_{\text{s}}\left(u'_s\right)^2 + M\left(1 + \tfrac{\phi_{\text{s}}}{\phi_\ell}\right)^2 u_s^2 \right] \mathrm{d}z$$

$$= \int_0^L \left[\hat{\mu}_{\text{s}} + \left(\tfrac{\phi_{\text{s}}}{\phi_\ell}\right)^2 \hat{\mu}_\ell \right] (u'_s)^2 + \left[\hat{\mu}_\ell\left(\left(\tfrac{\phi_{\text{s}}}{\phi_\ell}\right)'\right)^2 + M\left(1 + \tfrac{\phi_{\text{s}}}{\phi_\ell}\right)^2 \right] u_s^2 \, \mathrm{d}z$$

$$= \int_0^L \bar{\mu}(\phi_{\text{s}})(u'_s)^2 + \bar{M}(\phi_{\text{s}}, \phi'_{\text{s}}) u_s^2 \, \mathrm{d}z,$$

with $\bar{\mu} = \hat{\mu}_{\text{s}} + \left(\tfrac{\phi_{\text{s}}}{\phi_\ell}\right)^2 \hat{\mu}_\ell$ and $\bar{M} = \hat{\mu}_\ell\left(\left(\tfrac{\phi_{\text{s}}}{\phi_\ell}\right)'\right)^2 + M\left(1 + \tfrac{\phi_{\text{s}}}{\phi_\ell}\right)^2$. For $\phi_i \to 0$ one typically has $\hat{\mu}_i = \phi_i(\eta_i + o(1))$ and $M = m + o(1)$ with constant $\eta_i, m > 0$. Hence we have the uniform lower bound $\bar{M} \geq m$ but a linear degeneracy $\bar{\mu} = \eta_s \phi_{\text{s}} \to 0$ as $\phi_{\text{s}} \to 0$.

The corresponding derivative of the gravitational energy is

$$\frac{\mathrm{d}}{\mathrm{d}t} E_{\text{grav}} = \int_0^L zg(\varrho_{\text{s}} - \varrho_\ell)\partial_t \phi_{\text{s}} \, \mathrm{d}z = -\int_0^L zg(\varrho_{\text{s}} - \varrho_\ell)\partial_z(\phi_{\text{s}} u_{\text{s}}) \, \mathrm{d}z$$

$$= \int_0^L \phi_{\text{s}} u_{\text{s}} \partial_z(zg(\varrho_{\text{s}} - \varrho_\ell)) \, \mathrm{d}z = \langle \mathrm{D}E_{\text{grav}}(\phi_{\text{s}}), u_{\text{s}} \rangle.$$

Minimal dissipation gives the solution of the gradient system as the minimizer of

$$J(u_{\text{s}}; \phi_{\text{s}}) = \frac{1}{2}\mathcal{R}(u_{\text{s}}; \phi_{\text{s}}) + \langle \mathrm{D}E_{\text{grav}}(\phi_{\text{s}}), u_{\text{s}} \rangle \tag{6}$$

with respect to admissible solid velocity fields u_{s}. The Euler-Lagrange equations associated to this minimization problem are the following PDEs for the sedimentation problem

$$\partial_t \phi_{\text{s}} + \partial_z(\phi_{\text{s}} u_{\text{s}}) = 0, \tag{7a}$$

$$-\partial_z(\bar{\mu}\partial_z u_{\text{s}}) + \bar{M} u_{\text{s}} = -\phi_{\text{s}}\partial_z f_s, \tag{7b}$$

with $f_s = zg(\varrho_{\text{s}} - \varrho_\ell)$ and homogeneous Dirichlet boundary conditions $u_{\text{s}}(0) = u_{\text{s}}(L) = 0$ with the coefficient functions $\bar{\mu}, \bar{M}$ given above. In the dilute limit $\phi_{\text{s}} \to 0$ these coefficients simplify to $\bar{M} \sim m + o(1)$ and $\bar{\mu} = \phi_{\text{s}}(\eta_s + o(1))$ where $\eta_s = \frac{5\eta_\ell}{2}$ according to Einstein [32]. Note that in this model we completely eliminated any explicit dependence on ϕ_ℓ and $\mathbf{u}_\ell$. When the solid volume fraction approaches the maximal packing $\phi_{\text{s}} \to \phi_{\text{crit}}$, then the solid viscosity approaches infinty $\bar{\mu} \to \infty$ following the Krieger-Dougherty model

$$\bar{\mu} \sim (1 - \phi_{\text{s}}/\phi_{\text{crit}})^{-p}, \tag{8}$$

with different values of the exponent p, see [33, 34]. In the following we discuss several strategies to solve this 1D partial differential equation numerically in order to apply these concepts to the compressible Stokes equations in higher spatial dimensions.

4 Discretization of sedimentation model in 1D

4.1 Weak formulation

For given initial data $\phi_{\mathrm{s}}(t = 0, x) = \phi_0(x)$ and with boundary conditions $u_{\mathrm{s}}(t, 0) = u_{\mathrm{s}}(t, L) = 0$ we consider the system of hyperbolic-elliptic partial differential equations

$$\partial_t \phi_{\mathrm{s}} + \partial_z(\phi_{\mathrm{s}} u_{\mathrm{s}}) = 0, \tag{9a}$$

$$-\partial_z(\bar{\mu} \partial_z u_{\mathrm{s}}) + \bar{M} u_{\mathrm{s}} = -\phi_{\mathrm{s}} \partial_z f_s, \tag{9b}$$

$$f_s = \frac{\delta E}{\delta \phi_{\mathrm{s}}}, \tag{9c}$$

for $(t, z) \in (0, T) \times (0, L)$ using a given energy $E(\phi_{\mathrm{s}}) = E_{\mathrm{grav}}(\phi_{\mathrm{s}})$. To simplify the later finite element discretization we have introduced f_s as an additional auxiliary pressure-like variable.

In order to derive a weak formulation, we multiply (9) with appropriate test functions w_u, w_f, w_ϕ and in certain places integrate by parts. In the resulting weak formulation of (9) we seek a triple of functions $(u, \phi, f) \in U \times V \times V = X$ such that

$$\int_0^L \left(\bar{\mu} \partial_z u_{\mathrm{s}} \partial_z w_u + \bar{M} u_{\mathrm{s}} w_u \right) + \phi_{\mathrm{s}} w_u \partial_z f_s \, \mathrm{d}z = 0, \tag{10a}$$

$$\int_0^L \partial_t \phi_{\mathrm{s}} w_f - \phi_{\mathrm{s}} u_{\mathrm{s}} \partial_z w_f \, \mathrm{d}z = 0, \tag{10b}$$

$$\int_0^L f_s w_\phi \, \mathrm{d}z = \langle \mathrm{D}_{\phi_{\mathrm{s}}} E, w_\phi \rangle, \tag{10c}$$

for all $(w_u, w_f, w_\phi) \in X$.[1] Based on these spaces, let us define the following bilinear forms

$$a(u, v; \phi_{\mathrm{s}}) = \int_0^L \bar{\mu}(\phi_{\mathrm{s}}) \partial_z u \partial_z v + \bar{M}(\phi_{\mathrm{s}}) u v \, \mathrm{d}z, \tag{11a}$$

$$b(u, q; \phi_{\mathrm{s}}) = -\int_0^L \phi_{\mathrm{s}} u \partial_z q \, \mathrm{d}z, \tag{11b}$$

together with $(q, p) = \int_0^L q p \, \mathrm{d}z$ in V. Then this generates the following sligtly more compact weak formulation: Seek $\xi = (u_{\mathrm{s}}, f_s, \partial_t \phi_{\mathrm{s}}) \in X$ such that

$$a(u_{\mathrm{s}}, w_u) - b(w_u, f_s) + b(u_{\mathrm{s}}, w_f) + (\partial_t \phi_{\mathrm{s}}, w_f) + (f_s, w_\phi) = \langle \mathrm{D}E, w_\phi \rangle, \tag{12}$$

where will omit the parametric dependence of a, b on ϕ_{s} for clarity. If, for given ϕ_{s}, we define the associated operators $A : U \to U^*$, $B : U \to V^*$, $M : V \to V^*$ as $a(u, v) = \langle Au, v \rangle_U$, $b(u, f) = \langle Bu, f \rangle_V$, and $(q, p) = \langle Mq, p \rangle_V$, then we can write this system also in the typical form of a nested saddle point problem

$$L(\phi_{\mathrm{s}})\xi = \begin{pmatrix} A & -B^\top & 0 \\ B & 0 & M \\ 0 & M & 0 \end{pmatrix} \begin{pmatrix} u_s \\ f_s \\ \partial_t \phi_{\mathrm{s}} \end{pmatrix} = \begin{pmatrix} 0 \\ 0 \\ \mathrm{D}_{\phi_{\mathrm{s}}} E \end{pmatrix} \quad \text{in } X^*. \tag{13}$$

The weak formulation in the standard form (10) using bilinear forms (12) and using operators in (13) are formally equivalent.

---

[1] U denotes the Hilbert space for the velocities and V for the density and the pressure. If $\bar{\mu}$ and $\bar{M}$ was bounded away from zero and infinity, then one would expect $U = H^1(\Omega, \mathbb{R}^d)$ and $V = L^2(\Omega)$. However, since we are specifically interested in this degeneracy of $\bar{\mu}$ and $\bar{M}$ we are only going to specify their discrete subspaces U_h and V_h. For a more detailed analysis of this model and the underlying function spaces we refer to [26] and references therein.

4.2 Time-discretization, regularization and stabilization

First of all, note that the operators $A, B, \mathrm{D}_{\phi_\mathrm{s}}E$ in (13) generally depend on ϕ_s and thus the corresponding PDE system is nonlinear. Instead, when constructing a time-discretization we use finite differences to replace $\partial_t \phi_\mathrm{s} = \tau^{-1}(\phi_\mathrm{s}^{n+1} - \phi_\mathrm{s}^n)$ and can use an explicit dependence $A = A(\phi_\mathrm{s}^n)$, $B = B(\phi_\mathrm{s}^n), \mathrm{D}_{\phi_\mathrm{s}}E(\phi_\mathrm{s}^n)$, so that the resulting discretized equation is linear. The discretization in space is done using finite elements by choosing approriate subspaces $U_h \subset U$ and $V_h \subset V$. Alternatively one can also assume an implicit dependence of L on ϕ_s^{n+1} and solve the resulting discrete system $L\xi = (0, 0, \mathrm{D}E)^\top$ using a Newton iteration.

Upon close inspection of (13) note that the saddle point structure of the linearized system might require a Ladyzhenskaya-Babuška-Brezzi condition in order to ensure its well-posedness. This would need to be proven and the discretization would also have to use corresponding inf-sup stable finite element pairs U_h, V_h to construct $X_h = U_h \times V_h \times V_h$[2]. Alternatively, for the incompressible Navier-Stokes equation a similar mixed problem can also be stabilized by making the material slightly compressible. Similarly, here we introduce a stabilized operator L_stab of the form

$$
L_\mathrm{stab}(\phi_\mathrm{s}) = \begin{pmatrix} A & B^\top & 0 \\ B & 0 & M + \tau\varepsilon_\phi K^\phi \\ 0 & M & 0 \end{pmatrix}
\tag{14}
$$

where K^ϕ is an elliptic operator, which generates some extra regularity for ϕ_s. The time-discretization using L_stab reads

$$
L_\mathrm{stab}(\phi_\mathrm{s}) \begin{pmatrix} u_\mathrm{s} \\ f_s \\ \phi_\mathrm{s}^{n+1} \end{pmatrix} = \begin{pmatrix} 0 \\ M\phi_\mathrm{s}^n \\ \mathrm{D}_{\phi_\mathrm{s}}E \end{pmatrix}.
\tag{15}
$$

In the following we discuss further possible ways to stabilize the linearized operator L and to regularize the problem. By choosing $E(\phi_\mathrm{s}) = E_\mathrm{grav}(\phi_\mathrm{s}) + E_\mathrm{reg}(\phi_\mathrm{s})$ we can insert a regularization term into the equation. For the moment we consider

$$
E_\mathrm{reg}(\phi_\mathrm{s}) = \int_0^L \varepsilon_1 p^{-1}|\partial_z \phi_\mathrm{s}|^p + \varepsilon_2 |\phi|^2 \, \mathrm{d}z,
\tag{16}
$$

which gives rise to $f_s = (\varrho_\mathrm{s} - \varrho_\ell)gz - \varepsilon_1 \partial_z(|\partial_z \phi_\mathrm{s}|^{p-2}\partial_z \phi_\mathrm{s}) + \varepsilon_2 \phi_\mathrm{s}$. Terms of this type are very typical in hydrodynamic models of mixtures and give rise to Korteweg stresses. We are interested in the structure of the discrete equation and the limiting behavior of solutions as $\varepsilon_\phi, \varepsilon_1, \varepsilon_2 \to 0$. Note that due to a semi-implicit treatment of the gradient terms, other stabilizing terms will eventually appear in L_stab. For the discrete spaces U_h and V_h we are using vectorial and scalar $\mathbb{P}_1$ finite element discretizations, respectively. The importance of inf-sup conditions in compressible flows is discussed, for example, in [35] and similar viscous regularization approaches in the continuity equation of the compressible Stokes flows have been discussed already some time ago [36].

In the following we will investigate to extend these ideas to compressible flows for sedimentation and partially combine those ideas with the underlying energetic-variational structure to discretize the generalized Stokes problem using a Galerkin method.

---

[2]Note: For the moment we assume the space for w_f and w_ϕ to be the same. Using a mixed finite element formulation with different discrete spaces is possible in a straightforward manner.

5 Sedimentation experiments

In order to calibrate and validate the model, we perform sedimentation experiments in a Hele-Shaw cell of dimensions $L_{\text{width}} = 460\,\text{mm}$, $L_{\text{height}} = 310\,\text{mm}$ and $L_{\text{depth}} = 3\,\text{mm}$, see Figure 1. For the suspending liquid we use a silicon oil (PDMS, polydimethyl-siloxanes Korasilon fluid M1.000 by Kurt Obermeier GmbH, Germany) with a viscosity of $\mu_\ell = 10^0\,\text{Pa}\,\text{s}$ and a mass density of $\varrho_\ell = 998\,\text{kg}\,\text{m}^{-3}$. Molecular weight and siloxane chain length of this polymer is 26.500 and 358, respectively. As the suspended solid we use quartz glass beads (microspheres) with a radius of $R = 300 - 400\,\mu\text{m}$ so that $R/L_{\text{depth}} \sim 10^{-1}$. The particle mass density is $\varrho_s = 2500\,\text{kg}\,\text{m}^{-3}$. The experiment is prepared by letting particles settle so that they form a dense layer of $\phi_{\text{s}} \approx \phi_{\text{crit}}$ of uniform height. Then, the Hele-Shaw cell is turned quasi-instantaneously (within $< 1\,\text{s}$), so that particles start to sediment towards the bottom of the cell. We record optical images of one side of the cell at a resolution of $13\,\text{px/mm}$ and at a frequency of 1 Hz using a digital 12-bit monochrome CCD camera with 29 megapixels (LaVision Imager X-Lite 29M). To minimize reflections we use a set of polarizers. Based on the images we perform particle image velocimetry (PIV) in order to reconstruct the particle velocity field $\mathbf{u}_{\text{s}}$ from differences of consecutive images. We use the commercial PIV software Davis 10 (LaVision GmbH, Germany) employing a FFT-based digital image correlation technique. The resulting velocity field has a high spatial resolution (3.75 mm spacing between vectors), precision and accuracy (micrometer per second).
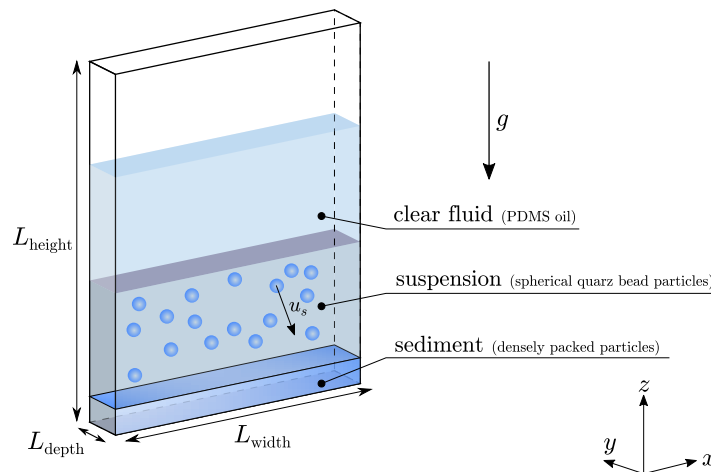

Figure 1: Hele-Shaw cell setup for sedimentation.

In Figure 3 snapshots of the experiments with reconstructed velocity vectors overlayed are shown at times $t = \{1, 2, 3, 4, 5, 6, 7, 8\} \times 10^3\,\text{s}$. In the first stages of the experiment $0 < t < 10^3\,\text{s}$ we observe the development of a characteristic Rayleigh-Taylor-like short-wavelength instability inducing a convective flow. While the particle Reynolds number is small $\text{Re} \sim 10^{-3}$, we observe a spatially nonuniform/unstratified flow and particle density. In the absence of any higher-order stabilizing effects, i.e., forces due to gradients of the density or surface tension, this instability is only resolved at the length-scale of the experimental setup, i.e., by particle radii and Hele-Shaw cell depth, and the effective dispersion viscosity. This granular Rayleigh-Taylor instability is well known and we refer to [11, 37, 38] and references therein for an overview of its relevance, modeling, and numerical treatment with discrete particle models. In these early stages the flow is not one-dimensional but has certain intrinsic higher-dimensional features. Furthermore, due to the small extension L_{depth} of the geometry in the y-direction, the flow field should have a distinct dependence on y. However, we assume that one can

derive an effectively two-dimensional model, where the finite-size of the Hele-Shaw cell is encoded in an effective dissipation $\mathcal{R} = \mathcal{R}_s + \mathcal{R}_\ell + \mathcal{R}_{\text{interact}} + \mathcal{R}_{\text{Hele-Shaw}}$ depending on $\mathbf{u}_s$ and $\mathbf{u}_\ell$ with

$$\mathcal{R}_{\text{Hele-Shaw}} = \int_\Omega M_s(\phi_s)|\mathbf{u}_s|^2 + M_\ell(\phi_s)|\mathbf{u}_\ell|^2 \, \mathrm{d}x \, \mathrm{d}z,$$

where for a clear fluid we have the standard gap-avergaged $M_\ell(0) = 12\mu L_{\text{depth}}^{-2}$. Such a model should certainly contain $\mathcal{R}_\ell$ with a singular viscosity μ_ℓ to prevent ϕ_ℓ from exceeding ϕ_{crit}. The values of M_ℓ, M_s are certainly finite, since the particle matrix still has a finite permeability k and thereby results in a flow rate given by Darcy's law. In this limit, our model becomes a system of Brinkman equations, which are commonly used to describe flow through a porous medium for a certain range of volume fractions, e.g. see [39].

At later times $t > 10^3 \, \text{s}$, the flow is almost unidirectional and mainly points in the z-direction. At this point in time, the volume fraction ϕ_s is decreasing in increasing z-direction, which renders the flow stable with respect to the Rayleigh-Taylor instability. In this stratified flow we observe three main regions of the concentration: a growing compact sediment layer at the bottom $0 < z < s(t)$, where $\phi_s \approx \phi_{\text{crit}}$ with $u_s = u_\ell \approx 0$, a layer where particles are actively sedimenting $s(t) < z < h(t)$ where $0 < \phi_s < \phi_{\text{crit}}$ and $u_\ell > 0$ and $u_s < 0$, and a top layer of clear fluid $\phi_s \approx 0$ for $h(t) < z < h_\infty$. While $s(t)$ is an increasing function of time, $h(t)$ decreases in time until the stationary solution $s \approx h$ is reached. In Figure 2 the x-averaged intensities of Figure 3 are shown and clearly indicate the progression of the settling process in time and the development of different spatial regions with high and low densities. In Figure 2 the function $s(t)$ is indicated using the red arrow, and the function $h(t)$ is indicated using the green arrow. Both curves $s(t)$ and $h(t)$ come together in the stationary state at time $t \approx 8000 \, \text{s}$, as indicated using the cyan arrow.
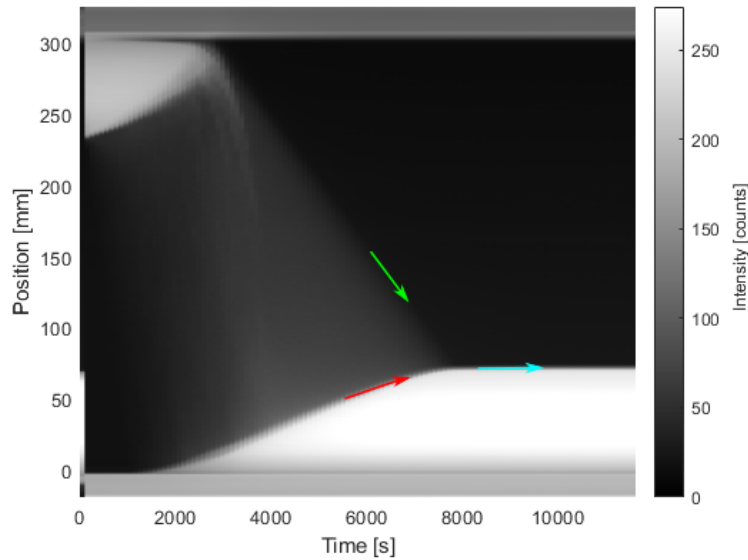

Figure 2: Average of intensity distribution in x-direction, which is proportional to density ϕ_s of the snapshots.

The slopes of these curves $s'(t)$ and $h'(t)$ correspond to shock speeds in the Kynch theory, related to the sedimentation flux by a Rankine-Hugoniot condition. Thereby, in general, experimental results as shown in Figure 2 can be used to construct the fluxes as discussed in [7]. In the following we discuss several numerical solutions obtained using the discretization in (14) and discuss different regularization approaches.
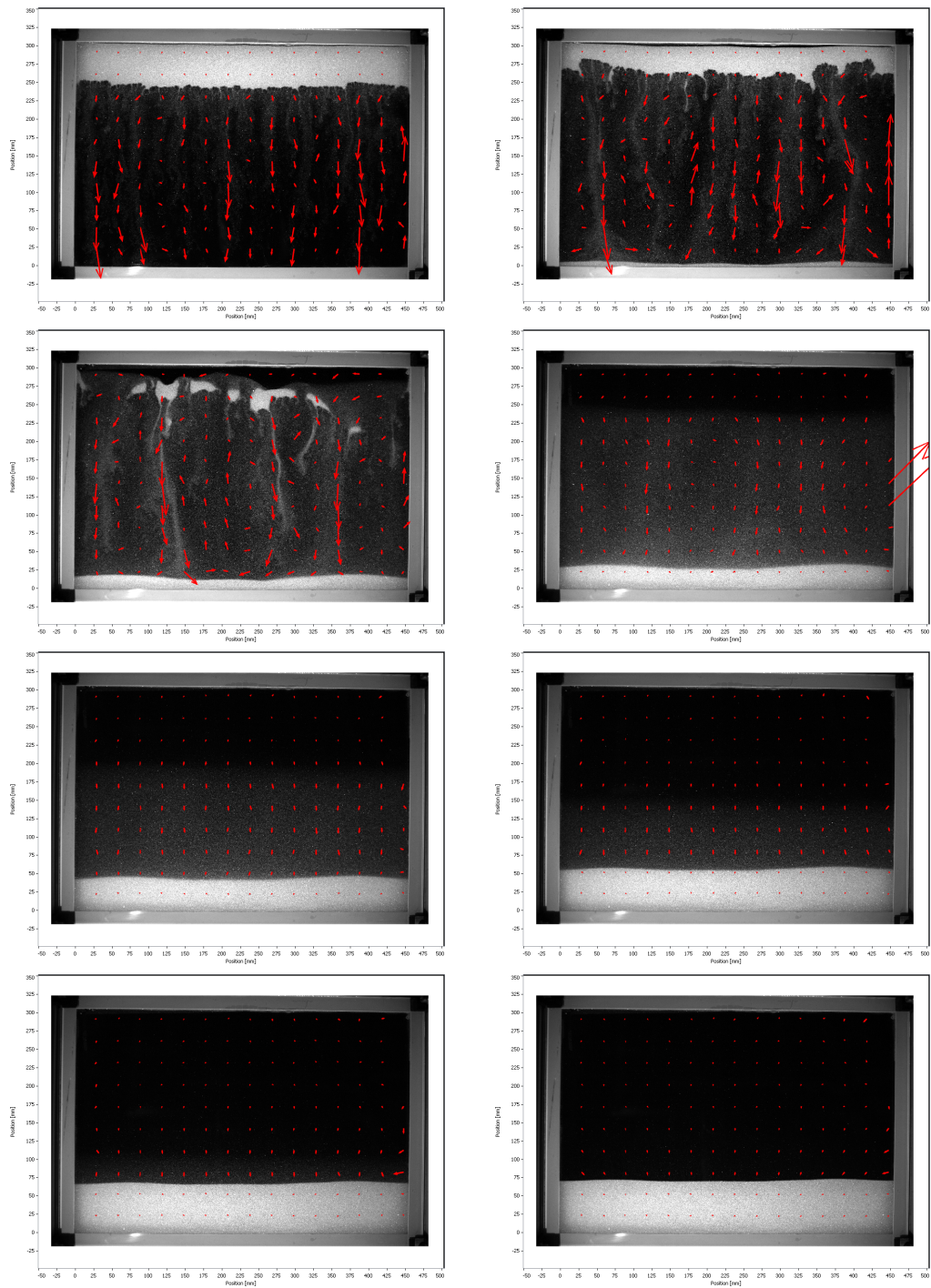
Figure 3: Sedimentation experiment in a Hele-Shaw cell starting at $t = 0$ from a compact $\phi_s \approx \phi_{crit}$ layer at $z \geq 250\,\mathrm{mm}$ presented at times $t = \{1, 2, 3, 4, 5, 6, 7, 8\} \times 10^3\,\mathrm{s}$ increasing times from left to right and top to bottom, where the color intensity indicates the density from black (low) to white (high) and the red vectors shows the velocity field reconstructed using particle image velocimetry (PIV).

6 Numerical experiments in 1D

For the numerical experiments using the sedimentation we let $L = 4$ and are using the materials laws

$$\bar{M}(\phi) = \left(1 + \tfrac{\phi}{(1-\phi)}\right)^2, \qquad \bar{\mu}(\phi) = \varepsilon + \mu|\phi| \left(1 + \tfrac{\nu}{(1-\phi)^2}\right), \tag{17}$$

in analogy to the Krieger-Dougherty law and the expression for $\bar{M}$ from the model reduction. When used in $d = 1$, the energy stabilization E_{reg} in (16) will have $p = 2$. For this set of simulations we never change the value of $\varepsilon = 10^{-4}$ but discuss the effect of the other regularizations. We consider two types of initial conditions $\phi_s(t = 0, z) = \phi_s^0(z)$ with

$$\phi_s^0(z) = \phi_0 + \frac{1 - 2\phi_0}{2}\left[1 + \tanh(100(z - z_0))\right], \tag{18a}$$

which for $\phi_0 \ll 1$ features a clear layer with $\phi_s \approx \phi_0$ for $0 < z < z_0$ and a dense layer with $\phi_s \approx 1 - \phi_0$ for $z_0 < z < L$. Alternatively we use

$$\phi_s^0(z) = \tfrac{1}{2}, \tag{18b}$$

to start from a uniform/stratified well-mixed layer. We will investigate the impact of different values of $\mu, \nu, \varepsilon_\phi, \varepsilon_1, \varepsilon_2$ on the numerical solution $\phi_s(t, z)$.

6.1 Densely packed initial data

Firstly, we discuss the sedimentation according to densely packed initial data as in (18a), where use $\phi_0 = 10^{-3}$ and $z_0 = \frac{16}{15}$. For large viscosity or $\phi_0 \to 0$ the sedimentation is rather slow because the particles need to be resuspended before they settle. This dependence of the time-scale on viscosity is shown in Figure 4, where with larger values of the viscosity coefficients ν the time-scale of sedimentation can be drastically increased. Note that increasing the viscosity ν also appears to have a regularizing effect, as can be seen in the increasing smoothness of the density profiles in Figure 4 going from panel (a) to (c).
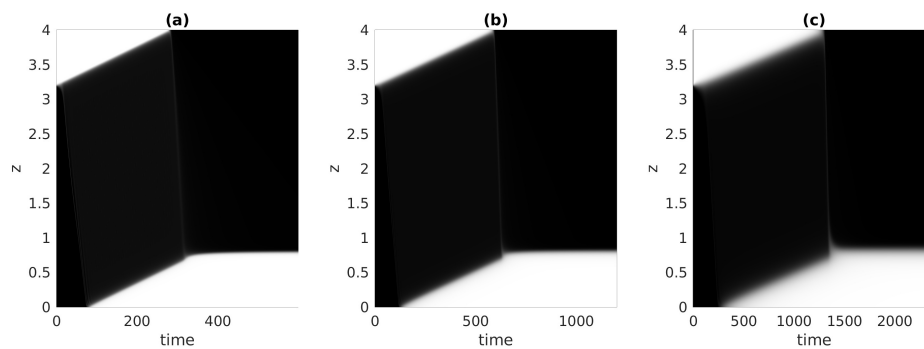

Figure 4: Sedimentation as a function of time with different ν. The parameters are $\varepsilon_1 = \varepsilon_2 = 0$, $\varepsilon_\phi = 2 \cdot 10^{-5}$, $\phi_0 = 10^{-3}$, $\mu = 1/5$ and (a) $\nu = 0.1$ (b) $\nu = 1$ and (c) $\nu = 10$.

Similarly, in Figure 5 we can also observe that the value of the regularization ε_ϕ in (14) has a strong influence on the time-scale for sedimentation. Stronger regularizations, i.e., larger values of ε_ϕ, enhance the resuspension and thereby accelerate the sedimentation process. Furthermore, as expected,

larger regularization parameters also lead to smoother concentration profiles in panel (a) compared to panel (c). While such a dependence on ε_ϕ is generally unwanted, this can be clearly related to the small value of ϕ_0 and corresponding zones of high concentration $\phi_s \approx 1$. Due to the high viscosity in these regions of high concentration, the time scale for the resuspension crucially depends on the regularization enhancing the resuspension.
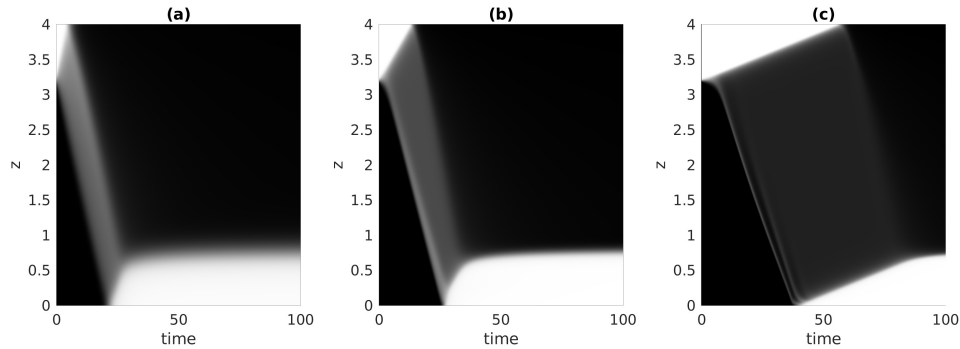

Figure 5: Sedimentation as a function of time with different ε_ϕ. The parameters are $\varepsilon_1 = \varepsilon_2 = 0$, $\phi_0 = 10^{-3}$, $\mu = 1/5$, $\nu = 0.02$ with (a) $\varepsilon_\phi = 10^{-2}$ (b) $\varepsilon_\phi = 10^{-3}$ and (c) $\varepsilon_\phi = 10^{-4}$.

In Figure 6 on can observe that the impact of different regularization parameters ε_ϕ is much less pronounced compared to the influence it shows in Figure 5. This clearly suggests that for sedimentation we can expect a certain level of dependence on the regularization parameter due to the fact that the regularization can enhance the resuspension of particles. Clearly, a very precise understanding of material laws and possible regularization mechanisms is necessary to be able to achieve any quantitative agreement with experimental measurements for densely packed initial data.
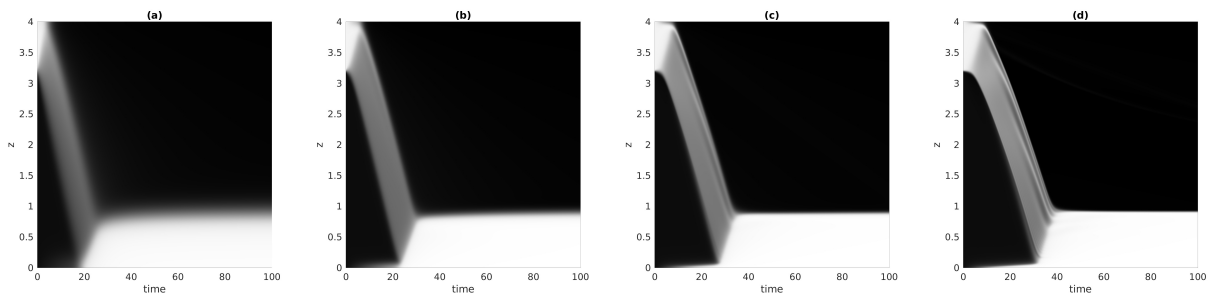

Figure 6: Sedimentation as a function of time with different ε_ϕ. The parameters are $\varepsilon_1 = \varepsilon_2 = 0$, $\phi_0 = 0.05$, $\mu = 1/5$, $\nu = 0.02$ with (a) $\varepsilon_\phi = 10^{-2}$ (b) $\varepsilon_\phi = 10^{-3}$ (c) $\varepsilon_\phi = 10^{-4}$ (d) $\varepsilon_\phi = 10^{-5}$.

6.2 Uniform initial data

Secondly, we discuss the sedimentation with uniform initial data as in (18b). With this stratefied initial data the granular Rayleigh-Taylor type instability is not present. This might even in one dimension imply stability for smaller regularization parameters. In Figure 7 one can see that all regularization schemes yield consistent results and only result in somewhat smoothened density profiles for (c) and (d) and a slight capillary overshoot in (d). The simulation without any regularization show slight instabilities where $\phi_s \approx 0$ visible in oscillations in the dark/gray areas for time $15 < t < 30$ and $2 < z < 3$.
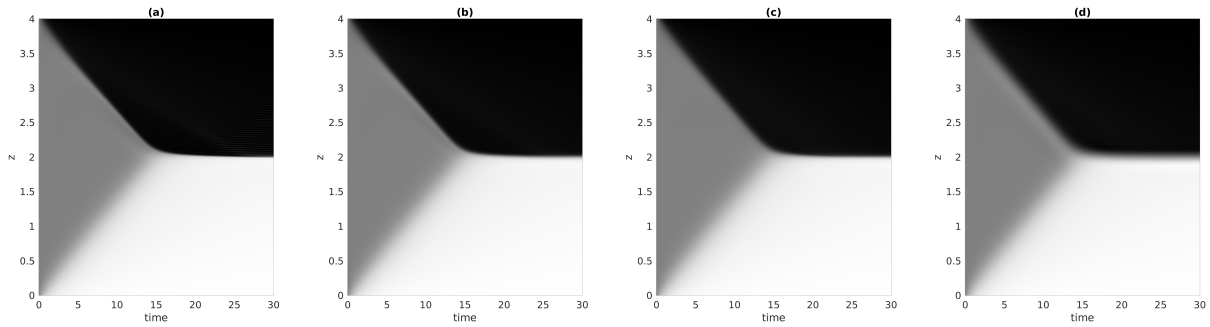
Figure 7: Sedimentation as a function of time with different regularizations. We use $\mu = 1/5$, $\nu = 1$ and (a) no regularization (b) $\varepsilon_\phi = 10^{-4}$ (c) $\varepsilon_2 = 5 \cdot 10^{-5}$ and (d) $\varepsilon_1 = 10^{-6}$.

Figure 8 shows the effect of using different viscosities without any other sources of regularization. One can see that, as expected, μ has a direct impact on the settling time but also affects the smoothness of the solution profiles ϕ_s, leaving the interpretation that the viscosity regularizes the hyperbolic evolution of the density, that would dominate the evolution with $\mu = 0$. A similar behavior can be observed when the parameter ν is changed for the solutions shown in Figure 9, which appears to also influence the final compactification of the sediment layer. Obviously, larger values the viscosity also lead to longer sedimentation times. In the limit of small regularization and small viscosity, the sedimentation is basically dominated by the interphase friction encoded in $\bar{M}$. Experimentally, one expects clear shock fronts in the $z - t$ density plots, which is quite similar to the experimental results shown in Figure 2. In such a situation the entire theory of hindered settling is encoded in $\bar{M} = \bar{M}(\phi_s)$, which one would need to determine from the experimental data.
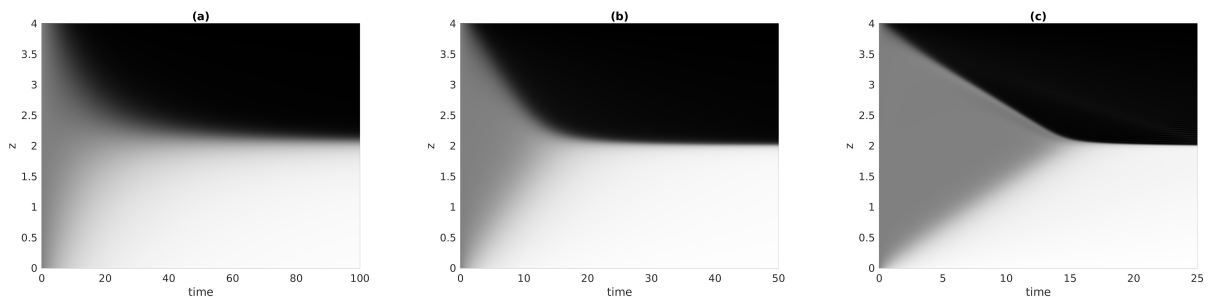

Figure 8: Sedimentation as a function of time with different viscosities μ. We use no regulariazion and $\nu = 1$ but (a) $\mu = 2$ (b) $\mu = 0.2$ (c) $\mu = 0.02$.
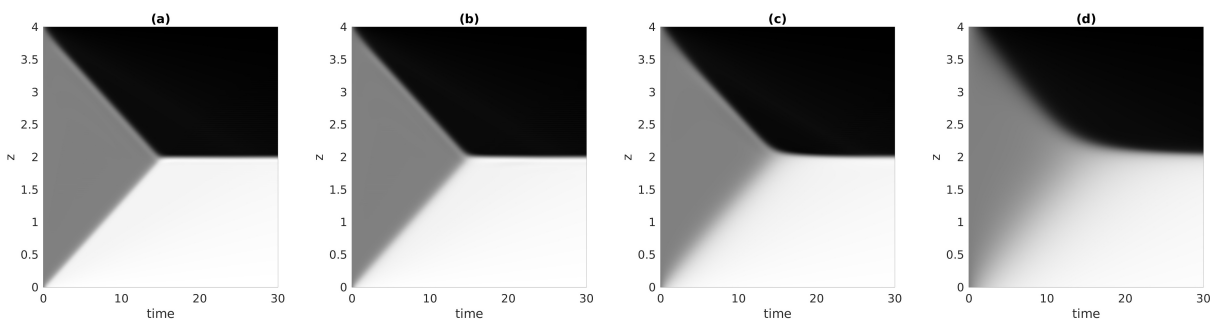

Figure 9: Sedimentation as a function of time with different viscosities ν. We use a regulariazion $\varepsilon_1 = 10^{-7}$, $\mu = 0.02$ and (a) $\nu = 10^{-2}$ (b) $\nu = 10^{-1}$ (c) $\nu = 1$ (d) $\nu = 10$.

6.3 Discussion of 1D results

Using a standard finite element discretization of the 1D sedimentation problem including diffusive and energetic regularization approaches, we numerically solve the sedimentation problem and obtain a good qualitative agreement when comparing the experimental results in Figure 2 with the equivalent theoretical predictions of this section, e.g. Figures 4,5,6 and Figures 7,8,9. While the discretization is free of oscillations indicative for the stability of the discretizations for positive densities and in the stratified regime, i.e. the density is nonincreasing with increasing z coordinate, the handling of the unstratified regime and of densities close to zero require the use of either diffusive or energetic regularizations using the parameters $\varepsilon_1, \varepsilon_2, \varepsilon_\phi$. While the experimental images in Figure 3 clearly show an initially fully developed two-dimensional flow and a granular Rayleigh-Taylor instability for $t < 3000\,\mathrm{s}$, the late stages $t > 3000\,\mathrm{s}$ of the settling process feature a unidirectional/stratified 1D flow where the settling model should be applicable. The general sharpness of the shocks visible in the averaged experimental profiles in Figure 2 indicate a flow, where regularization due to viscosity or gradient terms are negligible and $\bar{M}$ is the main dissipation mechanism controlling the dynamics. In [11] it is shown that viscosity is regularizing the Rayleigh-Taylor instability. Using similar methods as in [7], in this regime the PIV and intensity data should be used to identify the hindered settling function for a Hele-Shaw geometry, which is encoded in the function $\bar{M}(\phi_\mathrm{s})$.

7 Numerical experiments in 2D

The settling model of the previous section can be easily extended to a two-dimensional model, where it represents an energetic variational formulation of a compressible Stokes problem, which reads

$$\partial_t \phi_\mathrm{s} + \nabla \cdot (\phi_\mathrm{s}\mathbf{u}_\mathrm{s}) - \varepsilon_\phi \Delta \phi_\mathrm{s} = 0, \tag{19a}$$

$$-\nabla \cdot \sigma(\mathbf{u}_s) + \tilde{M}\mathbf{u}_s = -\phi_\mathrm{s}\nabla f_s, \tag{19b}$$

$$f_s = \frac{\delta E}{\delta \phi_\mathrm{s}}, \tag{19c}$$

with a diffusive regularization ε_ϕ, where the stress tensor σ for the compressible Stokes equation is of the form

$$\sigma(\mathbf{u}_\mathrm{s}) = 2\tilde{\mu}(\phi_\mathrm{s})e(\mathbf{u}_\mathrm{s}) + \tilde{\lambda}(\phi_\mathrm{s})(\nabla \cdot \mathbf{u}_\mathrm{s})\mathbb{I}, \tag{19d}$$

with density-dependent Lamé coefficient functions $\mu, \lambda > 0$. For the driving energy including an energetic regularization $\varepsilon_1, \varepsilon_2$ we use

$$E(\phi_\mathrm{s}) = \int_\Omega \left(\varepsilon_1 p^{-1}|\nabla \phi_\mathrm{s}|^p + (\varrho_s - \varrho_\ell)g\phi_\mathrm{s}z \right) \, \mathrm{d}x\,\mathrm{d}z, \tag{19e}$$

Note, this model is not an appropriate model for settling, since it does not satisfy the assumptions that lead to the derivation of the corresponding one-dimensional model. Nevertheless, we can use this model as a benchmark to discuss the impact of the different regularization approaches that we introduced before. The model (19) is discretized as before using finite elements with the two bilinear forms

$$a(\mathbf{u}, \mathbf{v}; \phi_\mathrm{s}) = \int_\Omega 2\tilde{\mu}(\phi_\mathrm{s})e(\mathbf{u}) : e(\mathbf{v}) + \tilde{\lambda}(\phi_\mathrm{s})(\nabla \cdot \mathbf{u})(\nabla \cdot \mathbf{v}) + \tilde{M}(\phi_\mathrm{s})\mathbf{u} \cdot \mathbf{v} \, \mathrm{d}x\,\mathrm{d}z, \tag{20}$$

$$b(\mathbf{u}, q; \phi_\mathrm{s}) = -\int_\Omega \phi_\mathrm{s}\mathbf{u} \cdot \nabla q \, \mathrm{d}x\,\mathrm{d}z, \tag{21}$$

which incorporates the fluid stress tensor σ by $a(\mathbf{u}, \mathbf{v}; \phi_s) = \int_\Omega \sigma(\mathbf{u}) : \nabla\mathbf{v} + \tilde{M}\mathbf{u} \cdot \mathbf{v}\, dx\, dz$. All other terms in the mixed weak formulation are entirely analogous to the previous weak formulation in (12). Furthermore, we mentioned ealier that in principle the mixed formulation would have to satisfy an inf-sup condition, whereas we use stabilization terms to enforce the well-posedness of the discrete problem. In two spatial dimensions we use the p-Laplace with $p = 3$ and solve the resulting nonlinear space-time discrete problem using Newton's method. For the Lamé parameter functions $\tilde{\mu}, \tilde{\lambda}$ we choose

$$\tilde{\mu}(\phi) = \varepsilon + \mu|\phi|\left(1 + \frac{\nu}{(1-\phi)^2}\right), \tag{22a}$$

$$\tilde{\lambda}(\phi) = \varepsilon + \lambda|\phi|\left(1 + \frac{\nu}{(1-\phi)^2}\right), \tag{22b}$$

and use $\varepsilon = 10^{-3}$ throughout all simulations. We are going to study the evolution of the compressible Stokes flow with $\phi_s(t = 0, x, z) = \phi_s^0(z - \frac{1}{40}\cos(4\pi x))$, $\phi_0 = 0.1$, $z_0 = 2/3$ with the dense and stratified initial data from (18) on the domain $\Omega = (0, 1)^2$. The sedimentation from dense initial data for energetic and viscous regularization is shown in Figure 10 and 11 respectively. Both simulations give consistent results but show slightly different amount of smoothing applied to the density profiles. Even with a timestep size of $\tau = 10^{-1}$, the final states of the simulation only violate these bounds $0 \leq \phi_s \leq 1$ slightly with $-\delta \leq \phi_s \leq 1 + \delta$ with $\delta = 10^{-2}$. The dependence of these bounds on time-discretization and regularization needs to be studied separately in the future. This is an interesting property of the discretization itself and should be studied theoretically, independent from the sedimentation. While the sedimentation shown in Figure 10 and 11 strongly depends on x, the short-wavelength pattern of the granular Rayleigh-Taylor instability is absent here, since this should be studied using the full two-phase model including the incompressibility constraint. It is discussed in the literature [40] that the Rayleigh-Taylor instability might be suppressed (or enhanced) for compressible Stokes flow.
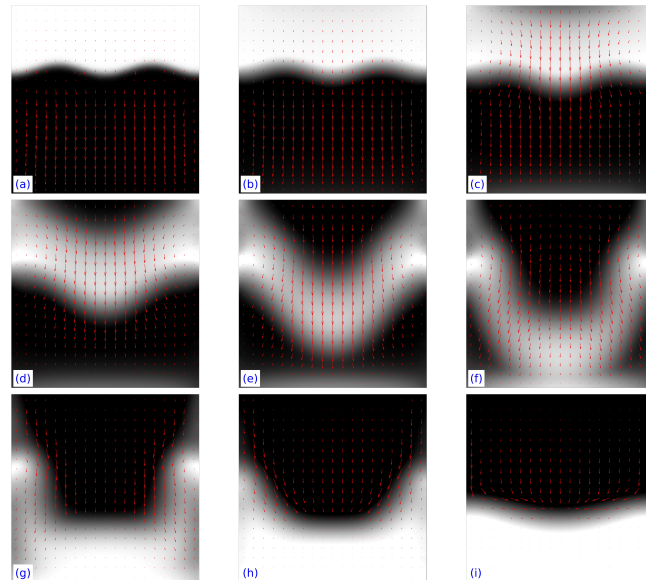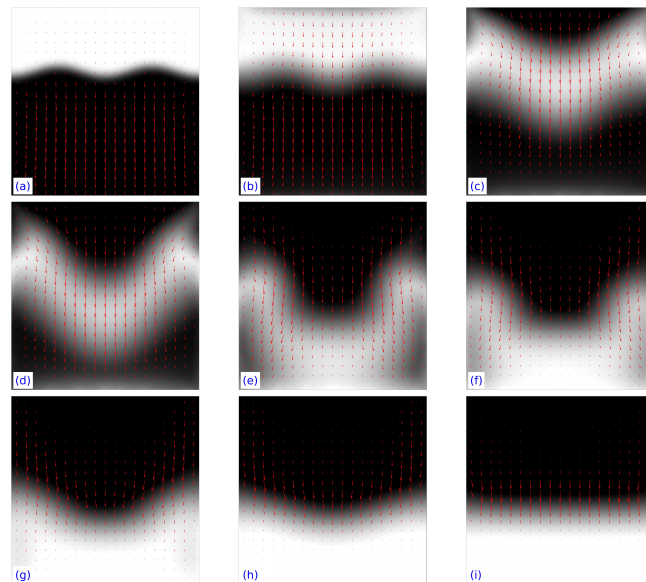

Figure 10: Solution of the compressible Stokes problem (19) with dense initial data (18a) at different times in increasing order (a,b,c,d,e,f,g,h,i). The shading indicates the density (white $\phi_s \sim 1$ and black $\phi_s \sim 0$) and red arrows indicate the flow field $\mathbf{u}_s$. We used $\mu = \lambda = 0.2$, $\nu = 0.5$, $\tilde{M} = 2$ and $\varepsilon_1 = 10^{-4}$, $\varepsilon_\phi = 0$.

Figure 11: Solution of the compressible Stokes problem (19) with dense initial data (18a) at different times in increasing order (a,b,c,d,e,f,g,h,i). The shading indicates the density (white $\phi_s \sim 1$ and black $\phi_s \sim 0$) and red arrows indicate the flow field $\mathbf{u}_s$. We used $\mu = \lambda = 0.2$, $\nu = 0.5$, $\tilde{M} = 2$ and $\varepsilon_\phi = 10^{-4}$, $\varepsilon_1 = 0$.
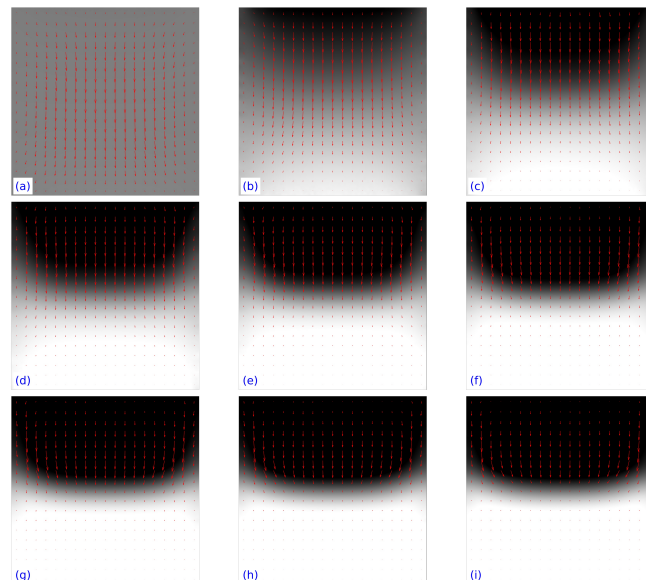

Figure 12: Solution of the compressible Stokes problem (19) with uniform initial data (18b) at different times in increasing order (a,b,c,d,e,f,g,h,i). The shading indicates the density (white $\phi_s \sim 1$ and black $\phi_s \sim 0$) and red arrows indicate the flow field $\mathbf{u}_s$. We used $\mu = \lambda = 0.2$, $\nu = 0.5$, $\tilde{M} = 2$ and $\varepsilon_1 = 10^{-4}$, $\varepsilon_\phi = 0$.
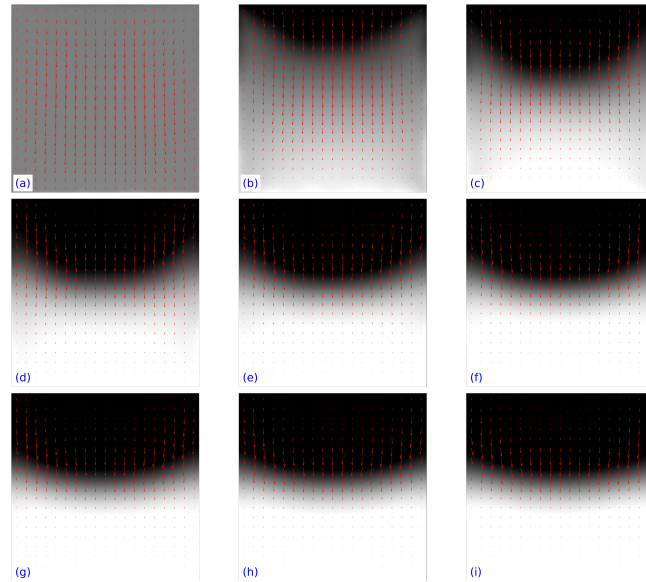
Figure 13: Solution of the compressible Stokes problem (19) with uniform initial data (18b) at different times in increasing order (a,b,c,d,e,f,g,h,i). The shading indicates the density (white $\phi_s \sim 1$ and black $\phi_s \sim 0$) and red arrows indicate the flow field $\mathbf{u}_s$. We used $\mu = \lambda = 0.2$, $\nu = 0.5$, $\tilde{M} = 2$ and $\varepsilon_\phi = 10^{-4}$, $\varepsilon_1 = 0$.

In Figure 12 and 12 we study the sedimentation from uniform initial data for the energetic and viscous regularization. Again, both solutions agree independent from the particular choosen regularization. What needs to be studied separately are the impliciations of the momentum balance in (19) in those zones, where $\phi_s \approx 0$ and the velocity is determined by a Darcy-type force balance $\tilde{M}(\phi_s)\mathbf{u}_s = -\phi_s \nabla f_s$. Here, the specific dependence of $\tilde{M}(\phi_s)$ as $\phi_s \to 0$ is certainly important. Similar to the experiments, when we use stratified initial data, then the solution also remains stratified with a minor x-dependence of the density due to the no-slip boundary conditions at the sidewalls $x = 0$ and $x = 1$.

8 Summary and conclusion

Using a variational formulation of two-phase flows for binary mixtures, we derive an effectively 1D model that describes the settling of particles. We discussed the time- and space-discretization of this model and we discuss the regularization and stabilization of the continuous and discrete model. The experimental results show the existence of the well-known short-wavelength granular Rayleigh-Taylor instability. We solve the corresponding compressible Stokes model using a viscous and an energetic regularization, where the latter generates higher-order Korteweg stresses in the momentum equation. We solve the sedimentation problem using various regularization parameters and compare the dynamics of particle densities (from experimentally averaged image intensities) with the theoretical predictions. For stratified flows, the results agree qualitatively well and are mostly independent of the choice of regularization, whereas the resuspension of dense suspensions can be greatly enhanced using a regularization so that it strongly affects the observed dynamics. We also study, to which extent viscosity has a regularizing character.

This study should help to understand the impact of regularization parameters for two-phase flows. Since the two-phase flow models used in practice to model suspensions are often prone to certain ill-posedness. In particular, a better understanding of physically-motivated regularization approaches

will be important in order to obtain qualitative and quantitative comparisons with experiments in future studies. Despite the fact that the Hele-Shaw geometry has a major impact on the settling dynamics, we think this is a good experimental setup to validate material laws $\bar{\mu}$ and $\bar{M}$ based on particle image velocimetry data.

References

[1] H.A. Einstein. *The bed-load function for sediment transportation in open channel flows*. Number 1026. US Government Printing Office, 1950.

[2] K.A. Landman, L.R. White, and M. Eberl. Pressure filtration of flocculated suspensions. *AIChE Journal*, 41(7):1687–1700, 1995.

[3] J.F. Richardson and W.N. Zaki. The sedimentation of a suspension of uniform spheres under conditions of viscous flow. *Chemical Engineering Science*, 3(2):65–73, 1954.

[4] R.H. Davis and A. Acrivos. Sedimentation of noncolloidal particles at low Reynolds numbers. *Annual Review of Fluid Mechanics*, 17(1):91–118, 1985.

[5] G.J. Kynch. A theory of sedimentation. *Transactions of the Faraday society*, 48:166–176, 1952.

[6] R. Bürger and W.L. Wendland. Sedimentation and suspension flows: Historical perspective and some recent developments. *Journal of Engineering Mathematics*, 41(2-3):101–116, 2001.

[7] R. Bürger, J. Careaga, and S. Diehl. A review of flux identification methods for models of sedimentation. *Water Science and Technology*, 03 2020.

[8] R. Bürger, F. Concha, and F.M. Tiller. Applications of the phenomenological theory to several published experimental cases of sedimentation processes. *Chemical Engineering Journal*, 80(1-3):105–117, 2000.

[9] D. Wan and S. Turek. An efficient multigrid-fem method for the simulation of solid–liquid two phase flows. *Journal of Computational and Applied Mathematics*, 203(2):561–580, 2007.

[10] R. Glowinski, T.-W. Pan, T.I. Hesla, D.D. Joseph, and J. Périaux. A distributed lagrange multiplier/fictitious domain method for flows around moving rigid bodies: application to particulate flow. *International Journal for Numerical Methods in Fluids*, 30(8):1043–1066, 1999.

[11] T.-W. Pan, D.D. Joseph, and R. Glowinski. Modelling Rayleigh–Taylor instability of a sedimenting suspension of several thousand circular particles in a direct numerical simulation. *Journal of Fluid Mechanics*, 434:23–37, 2001.

[12] P.R. Nott and J.F. Brady. Pressure-driven flow of suspensions: simulation and theory. *Journal of Fluid Mechanics*, 275:157–199, 1994.

[13] K. Gustavsson and J. Oppelstrup. Consolidation of concentrated suspensions–numerical simulations using a two-phase fluid model. *Computing and Visualization in Science*, 3(1-2):39–45, 2000.

[14] R. Rao, L. Mondy, A. Sun, and S. Altobelli. A numerical and experimental study of batch sedimentation and viscous resuspension. *International Journal for Numerical Methods in Fluids*, 39(6):465–483, 2002.

[15] Y.-J. Chou, F.-C. Wu, and W.-R. Shih. Toward numerical modeling of fine particle suspension using a two-way coupled Euler–Euler model: Part 2: Simulation of particle-induced Rayleigh–Taylor instability. *International Journal of Multiphase Flow*, 64:44–54, 2014.

[16] D. Leighton and A. Acrivos. The shear-induced migration of particles in concentrated suspensions. *Journal of Fluid Mechanics*, 181:415–439, 1987.

[17] D. Leighton and A. Acrivos. Measurement of shear-induced self-diffusion in concentrated suspensions of spheres. *Journal of Fluid Mechanics*, 177:109–131, 1987.

[18] J. F Morris and F. Boulay. Curvilinear flows of noncolloidal suspensions: The role of normal stresses. *Journal of rheology*, 43(5):1213–1237, 1999.

[19] P. Jop, Y. Forterre, and O. Pouliquen. A constitutive law for dense granular flows. *Nature*, 441(7094):727–730, 2006.

[20] F. Boyer, E. Guazzelli, and O. Pouliquen. Unifying suspension and granular rheology. *Physical Review Letters*, 107(18):188301, 2011.

[21] N. Murisic, B. Pausader, D. Peschka, and A.L. Bertozzi. Dynamics of particle settling and resuspension in viscous liquid films. *Journal of Fluid Mechanics*, 717:203–231, 2013.

[22] R.M. Höfer and J.J.L. Velázquez. The method of reflections, homogenization and screening for Poisson and Stokes equations in perforated domains. *Archive for Rational Mechanics and Analysis*, 227(3):1165–1221, 2018.

[23] B. Niethammer and R. Schubert. A local version of Einstein's formula for the effective viscosity of suspensions. *SIAM Journal on Mathematical Analysis*, 52(3):2561–2591, 2020.

[24] T. Ahnert, A. Münch, and B. Wagner. Models for the two-phase flow of concentrated suspensions. *European Journal of Applied Mathematics*, 30(3), 2018.

[25] D. Peschka, M. Thomas, T. Ahnert, A. Münch, and B. Wagner. Gradient structures for flows of concentrated suspensions. In *Topics in Applied Analysis and Optimisation*, pages 295–318. Springer, 2019.

[26] M.H. Farshbaf-Shaker and M. Thomas. Analysis of a compressible Stokes-flow with degenerating and singular viscosity. *WIAS Preprint*, 2020.

[27] D.A. Drew and S.L. Passman. *Theory of multicomponent fluids*, volume 135. Springer Science & Business Media, 2006.

[28] M. Ishii and T. Hibiki. *Thermo-fluid dynamics of two-phase flow*. Springer Science & Business Media, 2010.

[29] H. Abels, H. Garcke, and G. Grün. Thermodynamically consistent, frame indifferent diffuse interface models for incompressible two-phase flows with different densities. *Mathematical Models and Methods in Applied Sciences*, 22(03):1150013, 2012.

[30] S.S.L. Peppin, J.A.W. Elliott, and M.G. Worster. Pressure and relative motion in colloidal suspensions. *Physics of Fluids*, 17(5):053301, 2005.

[31] M.P. Ciamarra, A. Coniglio, and M. Nicodemi. Thermodynamics and statistical mechanics of dense granular media. *Physical Review Letters*, 97(15):158001, 2006.

[32] A. Einstein. *Eine neue Bestimmung der Moleküldimensionen*. PhD thesis, Universität Zürich, 1905.

[33] I.M. Krieger and T.J. Dougherty. A mechanism for non-Newtonian flow in suspensions of rigid spheres. *Transactions of the Society of Rheology*, 3(1):137–152, 1959.

[34] D. Quemada. Rheology of concentrated disperse systems and minimum energy dissipation principle. *Rheologica Acta*, 16(1):82–94, 1977.

[35] R.B. Kellogg and B. Liu. A finite element method for the compressible Stokes equations. *SIAM Journal on Numerical Analysis*, 33(2):780–788, 1996.

[36] O. Pironneau and J. Rappaz. Numerical analysis for compressible viscous isentropic stationary flows. *IMPACT of Computing in Science and Engineering*, 1(2):109–137, 1989.

[37] J.L. Vinningland, Ø. Johnsen, E.G. Flekkøy, R. Toussaint, and K.J. Måløy. Granular Rayleigh-Taylor instability: Experiments and simulations. *Physical Review Letters*, 99(4):048001, 2007.

[38] C. Völtz, W. Pesch, and I. Rehberg. Rayleigh-Taylor instability in a sedimenting suspension. *Physical Review E*, 65(1):011404, 2001.

[39] L. Durlofsky and J.F. Brady. Analysis of the Brinkman equation as a model for flow in porous media. *The Physics of Fluids*, 30(11):3329–3341, 1987.

[40] L. Baker. Compressible Rayleigh–Taylor instability. *The Physics of Fluids*, 26(4):950–952, 1983.